



# Surface plasmon quenched of near band edge emission and enhanced visible photocatalytic activity of Au@ZnO core-shell nanostructure



Mrinmoy Misra\*, Pawan Kapur, Madan Lal Singla

Material Research Division, Academy of Scientific & Innovative Research (AcSIR), Central Scientific Instruments Organisation, Sector 30 C, Chandigarh, India

## ARTICLE INFO

### Article history:

Received 28 August 2013

Received in revised form

30 December 2013

Accepted 4 January 2014

Available online 10 January 2014

### Keywords:

Core-shell

Nanostructure

Visible photo catalyst

Surface plasma resonance

Growth mechanism

## ABSTRACT

In this research work, we have demonstrated the synthesis of Au@ZnO core-shell nanostructure by a simple two-step chemical method. The ZnO coating enhance the charge separation process, whereas higher shell thickness suppresses the surface plasmon resonance (SPR) absorption of Au core and quenches the near band edge emission of ZnO. The photocatalytic activity of Au@ZnO nanostructure is evaluated by the degradation of methyl orange (MO) dye and oxidation of methanol under visible irradiation. Compared to pure ZnO nanoparticles (NPs), Au@ZnO core-shell NPs exhibit efficient plasmonic photocatalytic activity because of the presence of SPR in the Au core. The photocatalytic activity of the Au@ZnO core-shell NPs is enhanced by the shell thickness. Moreover, a possible mechanism for the photocatalytic activity of Au@ZnO under visible light irradiation is also proposed.

© 2014 Elsevier B.V. All rights reserved.

## 1. Introduction

In the last few years, semiconductor metal based core-shell structure has always attracted intensive research interest due to its unique optical and physical properties, which has universal potential applications in photo catalysis, solar cell and biological sensors [1–5]. Among several semiconductors, ZnO has the advantage of having large binding energy (60 eV), high band gap (3.37 eV), high photo catalyst activity, nontoxicity as well as physical and chemical stability [6–9]. However, due to the visible blindness and high rate of electron-hole recombination, its applications are somewhat restricted [10,11]. In order to enhance the photo catalytic performance with improved light harvesting efficiency, along with shift of Fermi level to more negative potential and to prolong the lifetime of photo generated carrier, modifications in ZnO has been explored through its composition with novel metals [12–24].

In the last few years, developments in nanoparticle synthesis allowed controllable preparation of a variety of hybrid metal-semiconductor nanostructures, such as metal coated semiconductor and core-shell heterostructure nanoparticles [25,26]. Among those available structures, metal-semiconductor core-shell structure has significant potential application as a photocatalyst. Furthermore, these structures have some advantages like having

the ability to enhance the efficiency of interfacial charge separation process and to achieve Fermi level equilibrium. Moreover, these structures have a controllable chemical composition and chemical stability, and are able to electrically insulate the metal nanoparticle from its surroundings. In core-shell structure, a very thin shell layer semiconductor in close proximity to the metal nanoparticle can also enhance the plasmonic features of the core-shell structure through plasmon-excitons coupling.

Recently, many synthesis routes have been developed to synthesize Au@ZnO core-shell nanostructure. Among the reported methods, the growth of gold nanoparticle and ZnO nanorods in atom beam co-sputtered Au-ZnO nanocomposite thin film was used to study the photoswitching behaviour [26]. Subsequently ZnO nanoflowers with gold nanoparticle were synthesized by hydrothermal method at 180 °C and the power conversion efficiency was studied [27]. Li and co-worker prepared Au-ZnO hybrid nanoparticles with a hexagonal pyramid-like structure and study the photocatalytic degradation of rhodamine B (RhB) under UV irradiation [28]. Yao and co-worker prepared Au-ZnO pyramid nanocrystals where Au particles were formed on the vertexes of ZnO nanopyramids and study the photocatalytic activity under UV irradiation [29]. Herring and co-worker prepared assembly of Au-ZnO nanopyramids using microwave irradiation (MWI) and study the mechanism of formation of the heterostructured nanopyramids [30].

But the relation between thickness and structure of ZnO shell to the morphology of final core-shell material and visible photo catalytic behaviour has not been investigated so far.

\* Corresponding author. Tel.: +91 9803473089; fax: +91 172 2657267.

E-mail address: [mrinmoymishra@gmail.com](mailto:mrinmoymishra@gmail.com) (M. Misra).

In this paper, we have proposed a fast and simple synthesis of core-shell nanoparticle containing gold as a core having tunable thickness of ZnO shell. It has been possible by varying the synthesis time of shell formation. Our studies further reveal that the thickness of the ZnO shell on each gold nanosphere has an effect on the structure and plasmonic fields of the final core-shell nano-materials. Subsequently, a model from these experimental results has been proposed to interpret the near bandgap edge emission quenching behaviour of such core-shell materials. The visible photocatalytic activities of ZnO nanoparticle and Au@ZnO core-shell structure with variable shell thickness were evaluated by the photocatalytic degradation of methyl orange (MO) and oxidation of methanol under visible light irradiation.

## 2. Experimental

### 2.1. Chemicals

All chemicals were of the highest purity available. Chloroauric acid trihydrate ( $\text{HAuCl}_4 \cdot 3\text{H}_2\text{O}$ ), zinc acetate and sodium hydroxide were used without further purification. DI water was taken from Millipore system.

### 2.2. Synthesis of gold nanoparticle

In this typical experiment, a 4 ml of 25 mM  $\text{HAuCl}_4$  was mixed with 100 ml of DI water, followed by the addition of 100  $\mu\text{l}$  of freshly prepared 0.1 M  $\text{NaBH}_4$  solution under vigorous stirring (1200 rpm). The colour of the solution changed from yellow to red. After 3 h the prepared gold solution was centrifuged, followed by removal of the supernatant and repeated washing with DI water. The precipitate was dispersed in 30 ml of DI water.

### 2.3. Synthesis of ZnO nanoparticle

In this typical synthesis, (0.01) M of zinc acetate was dissolved in 100 ml of DI water and (0.04) M of sodium hydroxide was dissolved in 100 ml of water separately. Then 20 ml of the prepared sodium hydroxide solution was mixed with 20 ml of the prepared zinc acetate solution in a drop-wise manner under vigorous stirring at a temperature of  $90^\circ\text{C}$  for 3 min. As a result, it was observed that the mixture turned into a whitish colloidal solution. The residue was separated from the reaction product using centrifugation, and was repeatedly washed using DI water.

### 2.4. Synthesis of Au@ZnO core-shell

For the synthesis of Au@ZnO core-shell nanostructure, a new colloidal method based approach is presented. An amount of 20 ml of previously prepared gold solution was mixed with 20 ml of 0.01 M zinc acetate solution under vigorous stirring. After 1 min, 20 ml of 0.04 M sodium hydroxide was added drop wise to the above solution under continuous stirring and a temperature of  $90^\circ\text{C}$  was maintained. The colour of the solution turned red to pink after adding sodium hydroxide. The precipitates were collected after intervals of 3 min and 5 min, respectively, and were named as S1 and S2. The collected samples were centrifuged at 8000 rpm and washed using DI water.

### 2.5. Characterization

The crystalline structure of nanoparticle samples were analyzed by an advanced X-ray diffractometer (XRD), using Ni-filter  $\text{Cu K}\alpha$  radiation at 40 kV and 40 mA in the  $2\theta$  range from  $20^\circ$  to  $80^\circ$  with a scan rate of  $0.02^\circ$  per second. The morphology

and structure of nanoparticles were characterized by Transmission Electron Microscopy (TEM). The photoluminescence spectra for liquid sample were investigated on Cary Eclipse fluorescence spectrophotometer. The UV-visible absorption measurement of aqueous colloidal solution was measured using Hitachi U-3900 H spectrophotometer.

## 3. Results and discussion

### 3.1. Surface morphology

Fig. 1(a–c) shows the typical transmission electron microscopy (TEM) image of the prepared gold nanoparticle and Au@ZnO core-shell nanoparticle at different magnifications. It can be seen that the surface of Au nanoparticles are smooth and spherical with a diameter of about 75–100 nm. To further understand the growth process, time-dependent chemical analysis on and around Au nanoparticle was carried out. It has been observed that in a core-shell nanoparticle, Au core is located at the centre of the particle. Further, after 3 m

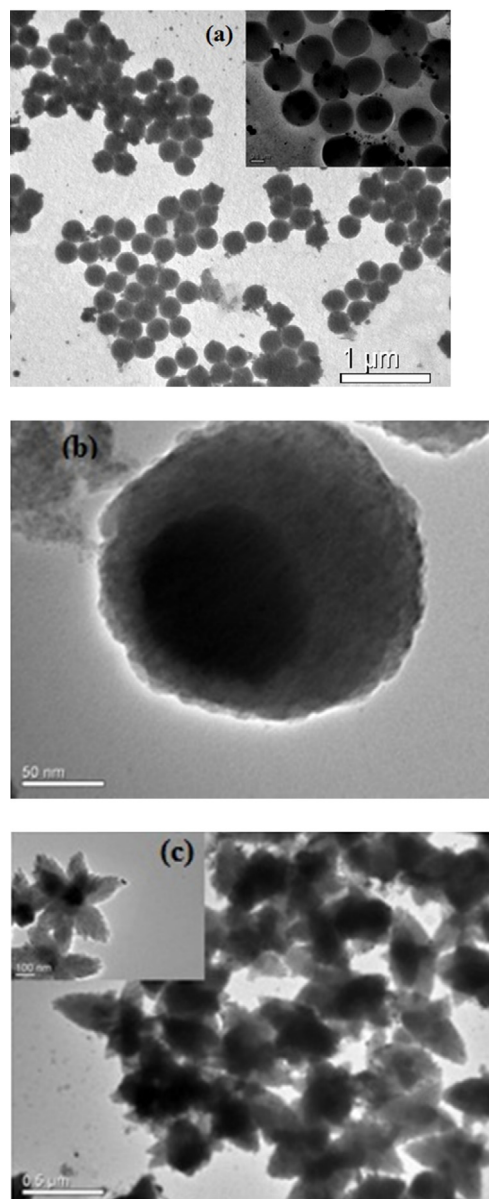


**Fig. 1.** (a) TEM of Au nanoparticles. (b) TEM of Au@ZnO nanoparticles after 3 m shell growth. (c) TEM of Au@ZnO nanoparticle after 5 m of shell growth.

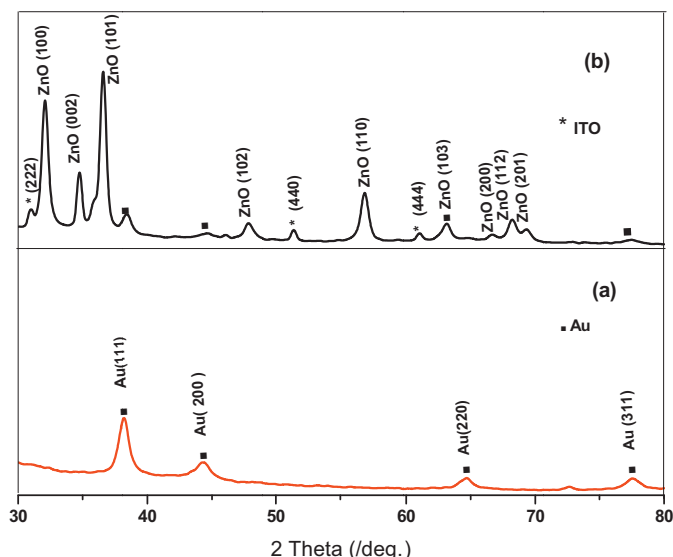


Fig. 2. X-ray diffraction (XRD) patterns of Au nanoparticles (a) and core-shell Au@ZnO nanoparticles (b).

of ZnO shell growth, a heterogeneous formation of ZnO nanoshell of 10 nm to 50 nm was visible, which got stabilized thereafter. After 5 m of shell growth, core-shell structure with ZnO antennae of about 100 to 150 nm in length was seen. The close interconnection between Au core and ZnO shell is believed to favour the transfer of photo-generated electrons from shell to core.

XRD pattern reveal characteristic diffraction peaks corresponding to (1 1 1), (2 0 0), (2 2 0), (3 1 1) of Au, which are located at angles  $2\theta = 38.17^\circ$ ,  $44.33^\circ$ ,  $64.68^\circ$  and  $77.54^\circ$ , respectively, reflecting the presence of Au as shown in Fig. 2(a). The  $d$  spacing of (1 1 1) fcc metallic Au is 0.235 nm (JCPDS no. 01-1174). Whereas in Au@ZnO core-shell nanostructure thin film, the ZnO peaks have been identified at angles  $31.71^\circ$ ,  $34.46^\circ$ ,  $36.34^\circ$ ,  $47.69^\circ$ ,  $57.78^\circ$ ,  $63.03^\circ$ ,  $66.64^\circ$ ,  $68.14^\circ$  and  $69.25^\circ$  corresponding to (1 0 0), (0 0 2), (1 0 1), (1 0 2), (1 1 0), (1 0 3), (2 0 0), (1 1 2) and (2 0 1), respectively, (JCPDS 36-1451,  $a = 0.325$  nm,  $c = 0.521$  nm), along with peaks due to gold nanoparticle, as shown in Fig. 2(b). There were some more ITO peaks identified at angles  $30.62^\circ$ ,  $35.42^\circ$ ,  $51.18^\circ$  and  $60.89^\circ$  corresponding to (2 2 2), (4 0 0), (4 4 0) and (4 4 4) (JCPDS 06-0416), respectively. From these results, it can be inferred that there exists an occurrence of a separate process within the radial shell, during the formation of ZnO shell layer, adjacent to the Au nanoparticle. After 3 m of synthesis, the (1 0 0) crystal plane of ZnO grow and stabilize the Au@ZnO heterojunction. It can be suggested that after the completion of the initial growth process, the wedge-shaped ZnO antenna begins to grow along the (1 0 1) direction as shown in Fig. 2(b). It appears that the Au@ZnO nanostructures are well

crystallized even though they were synthesised at a relatively low temperature of  $90^\circ\text{C}$ .

### 3.2. Growth mechanism of Au@ZnO core-shell

The crystal growth formation in aqueous solution can be explained in two stages: First crystal nucleation takes place, which is followed by crystal growth occurring from the crystal nuclei. The shape and size of nanostructures depend on the nucleation rate, orientation of crystals, as well as the crystal growth rate. Based on time dependent shell growth study, we observed that at the initial stage of nucleation, the crystal growth rate is fast because the ratio of  $\text{Zn}^+/\text{OH}^-$  is relatively high. As a result, single crystals aggregate together under the driving forces of surface energy and electrostatic force and a thin layer of ZnO shell with different nucleation centre formed on the surface of the spherical Au nanoparticle. As the ratio of  $\text{Zn}^+/\text{OH}^-$  gets depleted with time, the nucleation rate becomes low and the crystal growth rate being relatively high, results the adjacent nuclei to fuse together. The twinning of multiple nucleation sites at the onset of growth is responsible for creation of flower like Au@ZnO structures. The particles continue to grow, form wider antenna of ZnO, until the point of solubility is reached. The schematic of growth mechanism of Au@ZnO core-shell structure is given in Fig. 3.

When the metal nanoparticle makes contact with the semiconductor, it induces band-bending of the energy band of the semiconductor material. At the interface, a schottky barrier is formed, leading to an upward bending of the energy band of ZnO. Since the work function  $\theta_M$  of Au is higher than the electron affinity ( $\chi_S$ ) of ZnO, the barrier height ( $\theta_{SB}$ ) at the junction can be expressed by the given formula.

$$\theta_{SB} = \theta_M - \chi_S \quad (1)$$

where  $\theta_M = 5.1$  eV (Au) and  $\chi_S = 4.2$  eV (ZnO). Thus the barrier height ( $\theta_{SB}$ ) will be 0.9 eV. As a result, there will be a transfer of electrons between Au and ZnO until the Fermi level of both reach the same level [31,32].

Fig. 4 shows UV-vis spectra of ZnO NP, Au NP and Au@ZnO core-shell (varying thickness of shell) samples. It has been found that ZnO and gold nanostructures show absorption peaks at 360 nm and 530 nm, respectively.

The position of plasmon absorption of Au nanoparticles can be explained with the following equation:

$$\lambda_p = \left[ \frac{4\pi^2 c^2 m_{\text{eff}} \epsilon_0}{Ne^2} \right]^{1/2} \quad (2)$$

where  $m_{\text{eff}}$ ,  $N$  and  $e$  represent effective mass of free electron, electron density of the metal, and charge of electron, respectively.

In case of Au@ZnO core-shell structure (sample S1), the absorption peaks become broader and show two of them, one at 380 nm and the other at 512 nm. The former absorption peak results due to

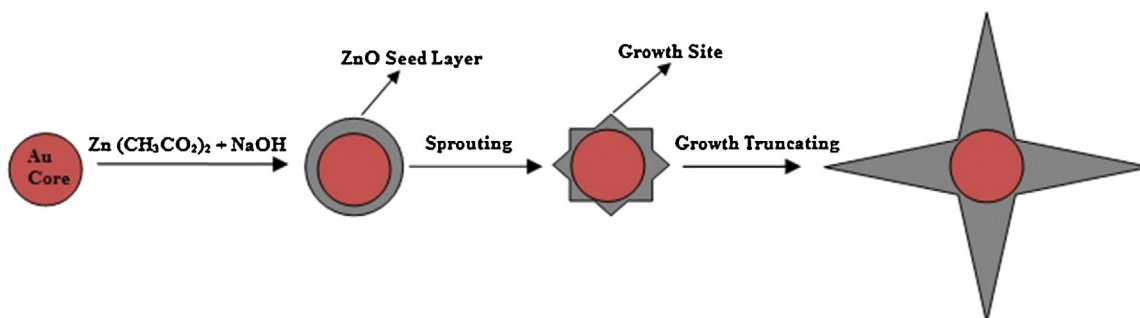
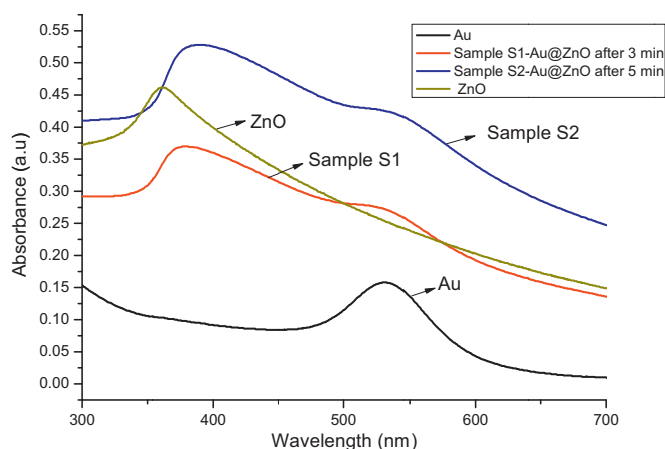


Fig. 3. Growth mechanism of Au@ZnO core-shell.



**Fig. 4.** Optical absorption spectra of ZnO, Au and Au@ZnO core-shell structure with variable shell thickness.

ZnO shell and the later due to gold core, respectively. The absorption spectra of ZnO shell in core-shell structure undergo a red-shift in comparison to ZnO nanoparticle, which attributes the formation of ZnO nucleation layer on the surface of Au nanoparticle. The absorption peak at 512 nm is attributed to the surface plasmon resonance (SPR) response of Au cores, and a significant blue-shift against pure Au nanocrystals is observed as the surface Plasmon generated electrons in Au get transferred to the conduction band of ZnO. The energy alignment mechanism is schematically plotted in Fig. 5

The SPR absorption of metal nanoparticles is highly sensitive to the surrounding environment. The surface Plasmon fringing field penetration depth  $Z$  of gold can be calculated as

$$Z = \left( \frac{\lambda}{2\pi} \right) \left[ \frac{(\epsilon_{\text{ZnO}} - \epsilon_{\text{Au}})}{\epsilon_{\text{ZnO}}^2} \right]^{1/2} \quad (3)$$

where  $\epsilon_{\text{ZnO}}$  and  $\epsilon_{\text{Au}}$  are the real parts of dielectric constant of ZnO and gold (Au), respectively [33]. In our sample (sample S1), the calculated plasmon fringing field penetration depth of gold core is 41 nm.

The Fermi level ( $E_F$ ) of the semiconductor can be represented by Eq (4) as:

$$E_F = E_{\text{CB}} + kT \ln \frac{n_c}{N_c} \quad (4)$$

where  $E_F$  is the Fermi level,  $E_{\text{CB}}$  is the conduction band energy level versus NHE,  $n_c$  is the density of accumulated electrons, and  $N_c$  is the charge carrier density of the semiconductor.

In order to study the energy band information at the surface, we have also studied the PL behaviour of all the samples. Generally ZnO exhibits two kinds of emissions: one is at the ultra violet

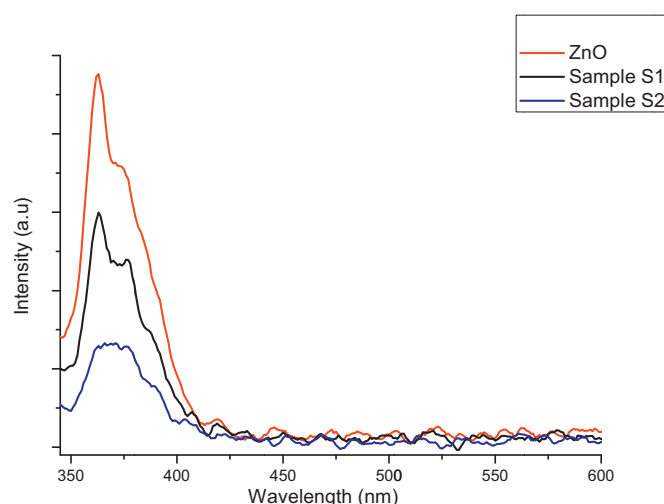


**Fig. 6.** Photoluminescence spectra of ZnO and Au@ZnO core-shell with variable shell thickness.

near band-edge emission in the UV region, and the other is at the visible region. The near band-edge emission is due to direct band gap transition and the visible emission is due to defects present in ZnO crystal. It is anticipated that in Au@ZnO core-shell structure, there will be a change in PL properties as compared to pure ZnO. When the ZnO colloidal solution is excited with 340 nm UV light, it shows a near band gap edge emission peak of 362 nm. As we have not found any emission peaks in the visible region, so it can be inferred that our ZnO nanocrystal was defect free as shown in Fig. 6. Whereas in the core-shell structure, when the ZnO shell is excited with UV light an electron-hole pair will be generated. The photo generated electron in the valence band (VB) can be excited to the conduction band (CB) with simultaneous generation of the same amount of holes that remain in the VB of ZnO. As the conduction band ( $E_c$ ) of ZnO is at a higher level than the Fermi level of gold ( $E_F$ ), it will facilitate the electrons to transfer from ZnO conduction band to gold core continuously until the two systems attain equilibrium. It enhances the charge separation and reduces the recombination of photo-induced electrons and holes and prolongs the lifetime of the electron-hole pairs. The resultant Fermi level of the core-shell shifts closer to the conduction band of ZnO. As a result, the near band emissions get quenched and reduce the recombination chances of photo-generated electrons with holes. The photo-induced holes can be trapped by surface-bound  $\text{H}_2\text{O}$  or  $\text{OH}^-$  to produce the hydroxyl radical species ( $\bullet\text{OH}$ ) [34–37]. These  $\bullet\text{OH}$  radicals are very powerful oxidants, which can attack dye molecules and can oxidize most of the pollutants. The accumulation of electrons in Au core can be summarised below.

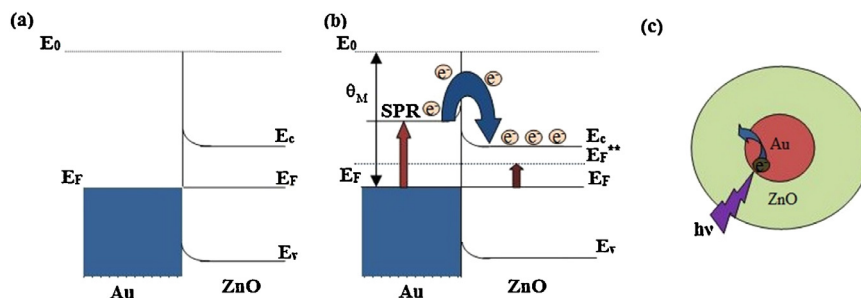


**Fig. 5.** The schematics of energy alignments mechanism of Au@ZnO core-shell nanostructure before SPR generation in Au (a), after SPR generation in Au (b) and the SPR generated electron transfer mechanism in Au@ZnO core-shell nanoparticle (c).



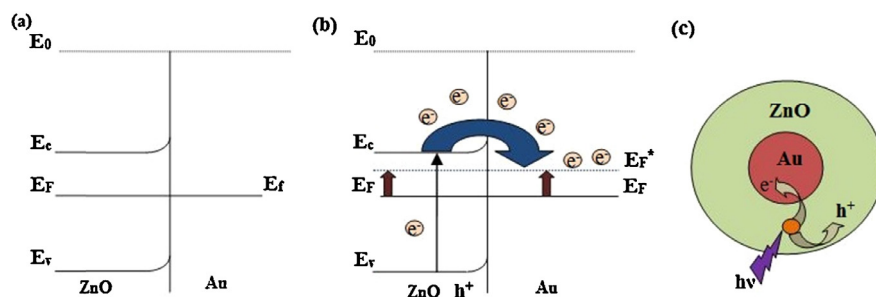
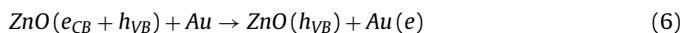


**Fig. 7.** Schematics of energy alignment of Au@ZnO nanoparticle before UV absorption (a), after UV absorption (b) and electron transfer mechanism of Au@ZnO core-shell nanoparticle under UV excitation (c).



It has also been observed that with increase of shell thickness, the band gap emission gets more quenched. Fig. 7 represents the schematics of energy alignment of Au@ZnO nanoparticle before UV absorption (a), after UV absorption (b) and electron transfer mechanism of Au@ZnO core-shell nanoparticle under UV excitation (c).

To study the photocatalytic activities of ZnO and Au@ZnO core-shell nanostructures, they were tested for Methyl orange degradation process under visible illumination. Methyl orange (MO) reveal one absorption band at 456 nm in the visible region. To study its photo degradation behaviour, we have measured the absorption of dye at 456 nm during the photocatalytic reaction process. To compare the photocatalytic activity more quantitatively, we have monitored the change in MO concentration ( $C$ ) relative to the initial concentration ( $C_0$ ). Fig. 8 represents the schematics of proposed visible light induced photocatalytic mechanism of Au@ZnO core-shell nanostructure (a) and kinetics of MO photodegradation by ZnO and Au@ZnO core-shell nanostructure with different shell thickness (b). The degradation curve for all the samples estimated as  $C/C_0$  versus time.

The degradation efficiency  $\eta$  (%) could be calculated as

$$\eta(\%) = \frac{C_0 - C}{C_0} \times 100 \quad (7)$$

where  $C_0$  is the initial concentration of dye and  $C$  is the concentration after photo irradiation.

In the absence of any catalyst, MO shows no change in absorption intensity upon visible illumination up to 200 min, a similar result has been reported in the case of Ag@Cu<sub>2</sub>O core-shell nanoparticle [38], whereas only 9% MO degrades in the presence of pure ZnO. The Au@ZnO core-shell NPs show enhanced

photocatalytic activity as compared to pure ZnO NPs, which can be attributed to the presence SPR of Au core. The photocatalytic activity Au@ZnO core-shell NPs were enhanced with an increase in shell thickness.

### 3.3. Time dependent visible photocatalytic activities

The photocatalytic activities of pure ZnO nanoparticle and Au@ZnO core-shell structure with variable shell thickness were evaluated by the photocatalytic degradation of methyl orange (MO) in an aqueous solution under visible light irradiation. A 150 W Xe lamp with a 390 nm cut-off filter was used as the visible light source. Prior to visible light exposure, 50 ml of MO (62 mM) and 5 mg of catalytic powder (ZnO or Au@ZnO) were magnetically stirred in the dark for 20 min to equilibrate the absorption and desorption of dye molecules. To monitor the degradation process, the absorption of pure MO solution, MO with ZnO or Au@ZnO was recorded after every 10 min at 456 nm.

### 3.4. Photocatalytic mechanism

The Au@ZnO core-shell nanoparticle show excellent photocatalytic activity on degradation of MO. The Au core act as a source of SPR generated electrons under visible illumination. The SPR generated  $e^-$  transfers to the conduction band of ZnO, where it gets trapped by electron acceptors such as adsorbed  $\text{O}_2$  to produce superoxide radical anions  $\text{O}_2^{\bullet-}$ . The oxidised positively charged Au nanoparticle capture  $e^-$  from water and dye molecule to neutralize the positive charge [39].

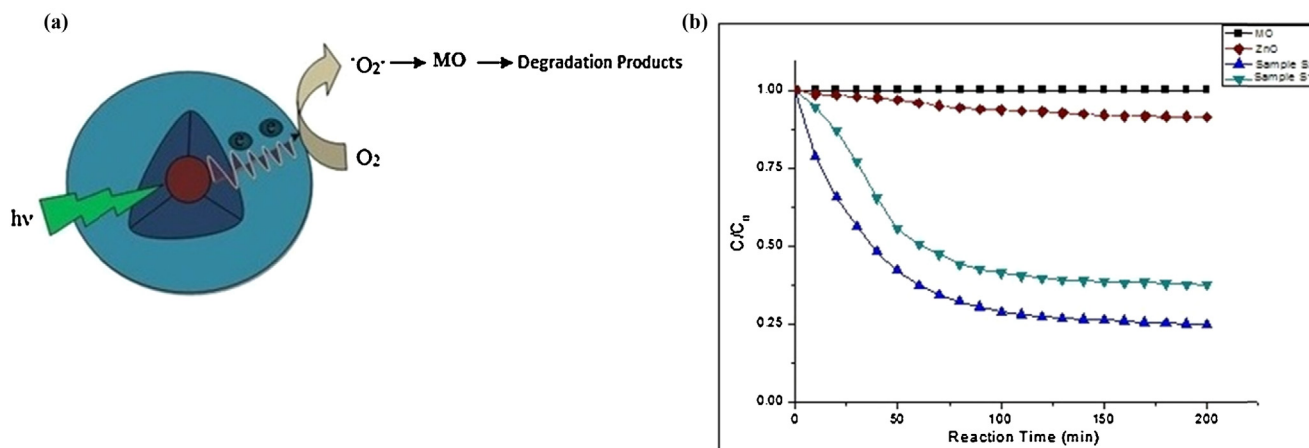


**Fig. 8.** Schematics of proposed visible Light Induced photocatalytic mechanism of Au@ZnO core-shell nanostructure (a) and Kinetics of MO photodegradation by ZnO and Au@ZnO core-shell nanostructure with different shell thickness (b).

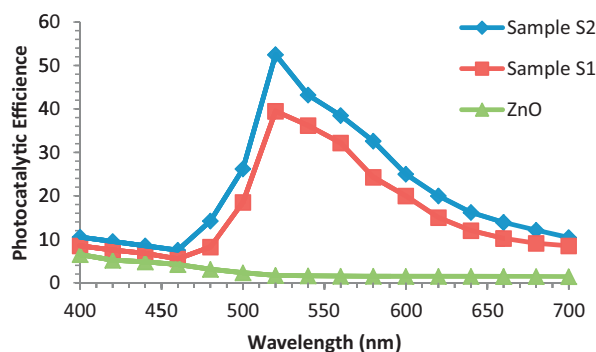
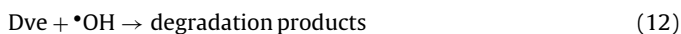
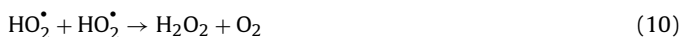


Fig. 9. Photocatalysis action spectra for the pure ZnO and the Au@ZnO core@shell NPs.



### 3.5. Wavelength dependent photocatalytic degradation of methyl orange dye

To study the wavelength dependent photocatalytic activity, all the samples were measured under monochromatic light using a 150 W Xenon (Hamamatsu Photonics L2482) lamp with UV cut-off filter as the light source coupled with a monochromator (Oriel Cornerstone 130 1/8 m). Prior to visible light exposure, 50 ml of MO (62 mM) and 5 mg of catalytic powder (ZnO or Au@ZnO) were magnetically stirred in the dark for 20 min to equilibrate the absorption and desorption of dye molecules. To monitor the degradation process at a particular wavelength, the absorption of MO with ZnO or Au@ZnO was recorded after every 30 min at 456 nm using Hitachi (U-3900 H).

Fig. 9 shows the photocatalytic action spectra for pure ZnO and the Au@ZnO core@shell NPs with deferent shell thicknesses. The pure ZnO exhibited negligible photocatalytic activity in the visible region, while the Au@ZnO nanoparticles showed significant enhancement at the wavelengths corresponding to the localised surface plasmon resonance (LSPR) of Au core. Under visible light excitation, the LSPR generated electrons get transferred to the conduction band of semiconductor to drive the chemical reaction. Therefore the SPR has a key influence on photo catalytic activity due to strong absorption between 510 to 530 nm. It has been observed that with an increase in shell thickness, the photocatalytic activity of Au@ZnO gets diminished. Very thin ZnO shell thickness will influence the lifetimes of charge carriers due to an increase in the surface states as compared to bulk states, thereby possibly reducing the photocatalytic efficiency of Au@ZnO core-shell nanoparticle.

### 3.6. Wavelength dependent methanol photo-oxidation

The activities of visible photocatalysts were also checked by methanol photo-oxidation by chromatographic analysis of generating carbon dioxide ( $\text{CO}_2$ ).  $\text{TiO}_2$  visible light catalytic oxidation of  $\text{HCOO}^-$  and  $\text{CH}_3\text{COOH}$  were evaluated by detecting  $\text{CO}_2$  as reported in the literature [40,41]. To study the wavelength dependent visible-light induced methanol oxidation activity, each of the catalysts (50 mg) were suspended in 100 ml aqueous solution of methanol (5 vol%, 5 ml) with same experimental set up as explained in case of wavelength dependent photocatalytic activity of MO

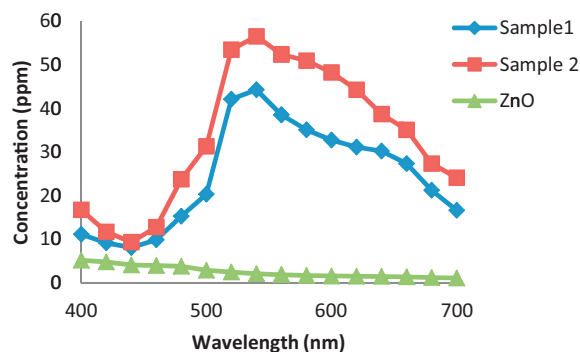


Fig. 10. Wavelength dependent oxidative decomposition of methanol under visible light.

degradation. During the irradiation of light at a particular wavelength, 100  $\mu\text{l}$  of the gas phase of reaction mixture was withdrawn with a syringe (Hamilton) and subjected to gas chromatographic analysis of carbon dioxide ( $\text{CO}_2$ ) (an Agilent 6890 equipped with a flame ionization detector and a methanizer). The methanizer was required for the enhancement of FID sensitivity by converting  $\text{CO}_2$  into methane.  $\text{N}_2$  was used as the carrier gas.

Au@ZnO core-shell nanoparticle exhibited photocatalytic activity under visible-light irradiation. Under visible irradiation, Au@ZnO core-shell structure with higher shell thickness showed higher levels of photocatalytic activity than lower ones. The highest level of photo catalytic activity under visible irradiation was observed in the range of 500–560 nm as shown in Fig. 10.

## 4. Conclusion

In summary, the Au@ZnO core-shell nanoparticle with flower shaped morphology has been synthesized successfully using chemical precipitation method. TEM and XRD results confirm the structure and orientation of growth of the nanoparticle. The photoluminescence spectra of ZnO and Au@ZnO suggest about the transfer of photogenerated electrons from ZnO shell to the gold nano particle. As a result, the near-band emission of ZnO gets quenched. In Au@ZnO nanostructure, the Au core increases the photocatalytic activity of ZnO, as confirmed by the degradation of methyl orange and oxidation of methanol under visible light irradiance.

## Acknowledgements

The authors acknowledge CSIR for research fellowships and supports extended for this work.

## References

- [1] S. Yang, D. Prendergast, J.B. Neaton, *Nano Letters* 12 (2011) 383–388.
- [2] M.R. Hoffmann, S.T. Martin, W. Choi, D.W. Bahnemann, *Chemical Reviews* 95 (1995) 69–96.
- [3] Z. Zhang, W. Wang, L. Wang, S. Sun, *ACS Applied Materials & Interfaces* 4 (2012) 593–597.
- [4] S. Yanagida, Y. Ishimaru, Y. Miyake, T. Shiragami, C. Pac, K. Hashimoto, T. Sakata, *Journal of Physical Chemistry* 93 (1989) 2576–2582.
- [5] K. Maeda, K. Teramura, T. Takata, M. Hara, N. Saito, K. Toda, Y. Inoue, H. Kobayashi, K. Domen, *Journal of Physical Chemistry B* 109 (2005) 20504–20510.
- [6] C.J. Wang, Z.L. Summers, Wang, *Nano Letters* 4 (2004) 423–426.
- [7] G. Malandrino, M. Blandino, M.E. Fragala, M. Losurdo, G. Bruno, *Journal of Physical Chemistry C* 112 (2008) 9595–9599.
- [8] S. Nair, A. Sasidharan, V.V. Divya Rani, D. Menon, S. Nair, K. Manzoor, S. Raina, *Journal of Materials Science Materials in Medicine* 20 (2009) 235–241.
- [9] B. Meyer, D. Marx, *Physical Review B: Condensed Matter* 67 (2003) 035403.
- [10] F. Zhang, Y. Ding, Y. Zhang, X. Zhang, Z.L. Wang, *ACS Nano* 6 (2012) 9229–9236.
- [11] W.-j. Sun, J. Li, G. Mele, Z.-q. Zhang, F.-x. Zhang, *Journal of Molecular Catalysis A: Chemical* 366 (2013) 84–91.

- [12] X.H. Xiao, F. Ren, X.D. Zhou, T.C. Peng, W. Wu, X.N. Peng, X.F. Yu, C.Z. Jiang, *Applied Physics Letters* 97 (2010) 071903–071909.
- [13] Y. Wei, J. Kong, L. Yang, L. Ke, H.R. Tan, H. Liu, Y. Huang, X.W. Sun, X. Lu, H. Du, *Journal of Materials Chemistry* 1 (2013) 5045–5052.
- [14] X. Yin, W. Que, D. Fei, F. Shen, Q. Guo, *Journal of Alloys and Compounds* 524 (2012) 13–21.
- [15] Q. Deng, X. Duan, D.H.L. Ng, H. Tang, Y. Yang, M. Kong, Z. Wu, W. Cai, G. Wang, *ACS Applied Materials & Interfaces* 4 (2012) 6030–6037.
- [16] A. Meng, S. Sun, Z. Li, J. Han, *Advanced Powder Technology* 24 (2013) 224–228.
- [17] M. Liu, S.W. Qu, W.W. Yu, S.Y. Bao, C.Y. Ma, Q.Y. Zhang, J. He, J.C. Jiang, E.I. Meletis, C.L. Chen, *Applied Physics Letters* 97 (2010) 231903–231906.
- [18] D. Lin, H. Wu, R. Zhang, W. Pan, *Chemistry of Materials* 21 (2009) 3479–3484.
- [19] E. Castillejos, E. Gallegos-Suarez, B. Bachiller-Baeza, R. Bacsa, P. Serp, A. Guerrero-Ruiz, I. Rodríguez-Ramos, *Catalysis Communications* 22 (2012) 79–82.
- [20] X. Liu, M.-H. Liu, Y.-C. Luo, C.-Y. Mou, S.D. Lin, H. Cheng, J.-M. Chen, J.-F. Lee, T.-S. Lin, *Journal of the American Chemical Society* 134 (2012) 10251–10258.
- [21] F. Xiao, F. Wang, X. Fu, Y. Zheng, *Journal of Materials Chemistry* 22 (2012) 2868–2877.
- [22] J. Kim, K. Yong, *Journal of Nanoparticle Research* 14 (2012) 1–10.
- [23] C.W. Lin, T.S. Pan, M.C. Chen, Y.J. Yang, Y. Tai, Y.F. Chen, *Applied Physics Letters* 99 (2011), 023303–023303.
- [24] F. Liao, Y. Huang, J. Ge, W. Zheng, K. Tedsree, P. Collier, X. Hong, S.C. Tsang, *Angewandte Chemie International Edition* 50 (2011) 2162–2165.
- [25] D.M. Schaadt, B. Feng, E.T. Yu, *Applied Physics Letters* 86 (2005) 063103–063106.
- [26] Y.K. Mishra, V.S.K. Chakravadhanula, V. Hrkac, S. Jebril, D.C. Agarwal, S. Mohapatra, D.K. Avasthi, L. Kienle, R. Adelung, *Journal of Applied Physics* 112 (2012) 064305–064308.
- [27] V. Dhas, S. Muduli, W. Lee, S.-H. Han, S. Ogale, *Applied Physics Letters* 93 (2008) 243103–243108.
- [28] P. Li, Z. Wei, T. Wu, Q. Peng, Y. Li, *Journal of the American Chemical Society* 133 (2011) 5660–5663.
- [29] K.X. Yao, X. Liu, L. Zhao, H.C. Zeng, Y. Han, *Nanoscale* 3 (2011) 4195–4200.
- [30] N.P. Herring, K. AbouZeid, M.B. Mohamed, J. Pinski, M.S. El-Shall, *Langmuir* 27 (2011) 15146–15154.
- [31] N.D. Orf, I.D. Baikie, O. Shapira, Y. Fink, *Applied Physics Letters* 94 (2009) 113503–113504.
- [32] D. Shao, M. Yu, H. Sun, T. Hu, J. Lian, S. Sawyer, *Nanoscale* 5 (2013) 3664–3667.
- [33] K. Okamoto, I. Niki, A. Shvarts, Y. Narukawa, T. Mukai, A. Scherer, *Nature Materials* 3 (2004) 601–605.
- [34] C. Gu, C. Cheng, H. Huang, T. Wong, N. Wang, T.-Y. Zhang, *Crystal Growth & Design* 9 (2009) 3278–3285.
- [35] T.-T. Yang, W.-T. Chen, Y.-J. Hsu, K.-H. Wei, T.-Y. Lin, T.-W. Lin, *Journal of Physical Chemistry C* 114 (2010) 11414–11420.
- [36] D.-H. Yu, X. Yu, C. Wang, X.-C. Liu, Y. Xing, *ACS Applied Materials & Interfaces* 4 (2012) 2781–2787.
- [37] L.A. Ghule, A.A. Patil, K.B. Sapnar, S.D. Dhole, K.M. Garadkar, *Toxicological & Environmental Chemistry* 93 (2011) 623–634.
- [38] J. Li, S.K. Cushing, J. Bright, F. Meng, T.R. Senty, P. Zheng, A.D. Bristow, N. Wu, *ACS Catalysis* 3 (2012) 47–51.
- [39] S.T. Kochuveedu, Y.H. Jang, D.H. Kim, *Chemical Society Reviews* 42 (2013) 8467–8493.
- [40] X. Yan, T. Ohno, K. Nishijima, R. Abe, B. Ohtani, *Chemical Physics Letters* 429 (2006) 606–610.
- [41] M. Mrowetz, W. Balcerski, A.J. Colussi, M.R. Hoffmann, *Journal of Physical Chemistry B* 108 (2004) 17269–17273.